RSC Advances

PAPER

View Article Online
View Journal | View Issue

Cite this: *RSC Adv.*, 2023, **13**, 22886

Synthesis of centimeter-size two-dimensional hybrid perovskite single crystals with tunable, pure, and stable luminescence

Haiyan Wang, *[ab] Qiaohe Wang,[a] Mengxin Ning,[a] Sen Li, [a] Renzhong Xue,[a] Peng Chen[a] and Zijiong Li[a]

The environment-friendly synthesis and property modulation of two-dimensional organic–inorganic halide perovskite (2D OHP) single crystals with large sizes and high quality are important for the fabrication of optoelectric devices. In this work, plate-like and centimeter-size $(BA)_2Pb(Br_xI_{1-x})_4$ (BA = *n*-butylammonium, *x*: 0–1) single crystals with high crystallinity were synthesized *via* the cooling crystallization method in a mixed HX (X: I, Br) acid aqueous solution. The synthesized samples were single-phase with homogenously distributed Br and I ions. The lattice structure and bandgap of $(BA)_2Pb(Br_xI_{1-x})_4$ were both finely tuned through halide alloying. Pure photoluminescence with unitary wavelength was obtained in the mixed-halide samples compared to those of monohalides $(BA)_2PbI_4$ and $(BA)_2PbBr_4$. This is attributed to the structural homogeneity of the alloyed crystals. Moreover, the prepared $(BA)_2Pb(Br_xI_{1-x})_4$ samples showed higher photo and thermal stability for a long duration even with ion migration. This study will be an important reference for the fabrication and property modulation of 2D OHP-based light-emitting and other optoelectric devices.

Received 28th April 2023
Accepted 27th June 2023

DOI: 10.1039/d3ra02816j

rsc.li/rsc-advances

1. Introduction

Two-dimensional organic–inorganic halide perovskites (2D OHPs) with a layer-to-layer structure are considered bread slices owing to their three-dimensional (3D) parent structures with long chains or large-size alkylammonium ligands.[1] The dielectric alkylammonium unit in 2D OHPs confines the carrier in the inorganic layer to form a quantum well. This unique electronic structure endows 2D OHPs with unique properties including high exciton binding energy,[2–4] photoluminescent quantum yield (PLQY),[5,6] anisotropy,[7–9] and outstanding stability.[10–12] Thus, based on the above-mentioned advantages, 2D OHP films and single crystals are considered potential candidates for the fabrication of photo/X-ray detectors,[13–17] light-emitting devices,[18–20] and photovoltaic cells.[21,22]

2D OHP single crystals (2D OHP SCs) possess better optical and electronic properties than polycrystalline films owing to their low density of defects and high carrier transport capacity. Therefore, the fabrication and property modulation of large-size and high-quality 2D OHP SCs have attracted increasing attention. 2D OHP SCs are mainly synthesized *via* solution methods using organic solvents such as dimethylformamide and dimethyl sulfoxide,[15,16,23,24] which are toxic to the environment, limiting the application of 2D OHP SC-based devices. Alternatively, the use of water as a solvent affects the solubility and crystallization temperature of different OHPs, leading to the formation of OHP alloys with different compositions; the product content cannot be controlled, especially for heavily mixed perovskites.[25–27] Therefore, it is urgent to develop methods for the fabrication of 2D OHP SCs with tunable performances and a stable phase structure in a nontoxic aqueous solution.

The overlapping orbitals of a metal cation and halide anion dictate the electronic structure of OHPs. Hence, halide mixing is an effective way to modulate the bandgap and light emission wavelength of OHPs. A large halide has small bandgap energy, and consequently broad range of colors is emitted using mixed-halide perovskites (MHPs) as emitters.[28–31] Halide mixing regulates the light emission of 2D OHPs through the lattice distortion of octahedral $[PbX_6]^{4-}$ (X = halide). It has been verified that lattice distortion induces broadband white-light emission in layered OHPs by introducing self-trapped excitons (STEs).[32–35] STE related to electron–phonon coupling is dependent on the distance between the inorganic layers.[36] However, the influence of lattice distortion on the distance of the neighboring inorganic layers and the consequent emission property of 2D OHPs has attracted limited attention.

Presently, halide ion migration in MHP emitters is still not well understood. Different halides migrating in opposite directions result in phase separation and the spectral instability of MHPs.[37,38] Ion migration in 3D MHPs has been widely

[a]*College of Physics and Electronic Engineering, Zhengzhou University of Light Industry, Zhengzhou 450002, PR China. E-mail: wanghaiyan@zzuli.edu.cn*

[b]*Henan Key Laboratory of Magnetoelectronic Information Functional Materials, Zhengzhou University of Light Industry, Zhengzhou 450002, PR China*

studied, whereas the study of 2D MHPs is scarce. Low-dimensional perovskites can suppress halide ion migration because of the intercalated spacer ligands.[39] The results of density functional theory also indicated that octahedral distortions significantly hinder bromide migration along the out-of-plane direction in Br–I mixed 2D MHPs.[40] Thus, systematic exploration is required to study the specific effect of lattice distortion in ion migration and the spectral stability of 2D MHPs. The fabrication of 2D MHP SCs and evaluation of their luminescent characteristics with lattice structure evolution can be performed by studying 2D OHPs for their application in commercial light-emitting diodes (LEDs).

In this study, centimeter-size 2D $(BA)_2Pb(Br_xI_{1-x})_4$ ($x = 0$–1) single crystals were fabricated in an aqueous solution by designing the solution composition and the cooling procedure. Subsequently, a systematic study was performed by focusing on the chemical composition, crystal structure, bandgap, and light-emission properties of the multiple-halide 2D OHP crystals. The compositional deviation between the prepared $(BA)_2Pb(Br_xI_{1-x})_4$ crystals and precursor solutions was measured and analyzed in detail. The tunable lattice structure and the bandgap of samples were detected. Further, the unique photoluminescent characteristics and excellent stability of the $(BA)_2Pb(Br_xI_{1-x})_4$ alloys were explored for their application in light-emitting devices. This study will be an important reference for the fabrication and property tuning of 2D OHP-based light-emitting and other optoelectric devices.

2. Experimental details

2.1 Synthesis of MHP single crystals

2.1.1. $(BA)_2Pb(Br_xI_{1-x})_4$ single crystals. 2.5 mmol of PbO powder was added to a mixed solution of hydroiodic acid (HI, 46.21%) and hydrobromic acid (HBr, 48%). A total of 40 mmol of HI and HBr was taken. Then, 0.9 mL of hypophosphoric acid (H_3PO_2, 54%) was added as a stabilizer to the above solution to form solution A. Solution A was heated at 100 °C for 30 min under stirring to dissolve the PbO powder completely. In another set, 5 mmol of *n*-butylamine ($C_4H_{11}N$, 99.5%) was slowly added dropwise to a mixed solution of HI and HBr to form solution B. The total quantity of HI and HBr was 5 mmol in solution B, and the ratio of HI : HBr was kept consistent with that of solution A. Then solution B was added dropwise to solution A to form solution C. Solution C was heated at 140 °C for 20 min, and then cooled from 140 °C to 20 °C at a rate of 5 °C h^{-1}. The mixed-halide $(BA)_2Pb(Br_xI_{1-x})_4$ single crystal was filtered and vacuum dried in a freezer dryer.

2.1.2. $(BA)_2Pb(Cl_xBr_{1-x})_4$ single crystal. The process for the fabrication of the $(BA)_2Pb(Br–Cl)_4$ single crystal was the same as that for the $(BA)_2Pb(Br_xI_{1-x})_4$ single crystal, except that chlorhydric acid (HCl, 35%) was used in the place of hydroiodic acid (HI, 46.21%).

2.2 Characterization

The morphology and crystallinity of the samples were detected *via* field emission scanning electron microscopy (FE-SEM, JSM-7001F, Japan), X-ray diffraction spectrometry (XRD, SmartLab SE, China), and high-resolution transmission electron microscopy (HR-TEM, Philips CM-20 microscope). The XRD instrument was operated at a voltage of 40 kV and 50 mA current, and Cu-Kα radiation ($\lambda = 1.5406$ Å) was used as the X-ray source. XRD patterns were recorded in the 2θ range of 5° to 70° at a scan rate of 5° min^{-1} with the energy step of 0.02°. Energy dispersive X-ray spectroscopy (EDS) was used to measure the doping efficiency of the second halide and the homogeneity of the alloy by scanning an area of 25×25 μm^2. The chemical composition of the products was analyzed through X-ray photoelectron spectroscopy (XPS, ESCALAB 250 Xi) using Al-Kα radiation with an energy of 1486.6 eV, beam size of 500 μm, pass energy setting of 40 eV and energy step of 0.1 eV. The bandgap and emission of the samples were measured using a UV-visible spectrophotometer (UH4150, China) and a fluorescence spectrometer (Horiba; Fluoro Max-4) with an integrated sphere (Horiba; Quanta-φ), respectively, at room temperature. The photo and thermal stability of the synthesized $(BA)_2Pb(Br_xI_{1-x})_4$ were executed using a UV lamp and hot stage, respectively.

3. Results and discussion

3.1 Morphology and structure

Different colors of plate-like centimeter-size $(BA)_2Pb(Br_xI_{1-x})_4$ single crystals grew in the mixed HX acid aqueous solutions. The method for the synthesis of the crystals is shown in Fig. 1(a). The morphology of the synthesized $(BA)_2PbI_4$, $(BA)_2Pb(Br_{0.8}I_{0.2})_4$, and $(BA)_2PbBr_4$ single crystals grown in pure HI, HI + HBr, and pure HBr acids, respectively, is shown in Fig. 1(b). The surface morphology of the samples was observed using an optical microscope. Fig. 1(c) shows the layered structure of the $(BA)_2PbI_4$ crystal, which was also observed in the other $(BA)_2Pb(Br_xI_{1-x})_4$ samples.

Fig. 2(a) shows the powder XRD patterns of the synthesized $(BA)_2Pb(Br_xI_{1-x})_4$. The series of well-defined periodic diffraction peaks assigned to the (00*n*, $n = 1, 2, 3\ldots$) lattice planes demonstrates the orientation of the high growth. The small full width at half maximum (FWHM) of the (001) plane proves the excellent crystalline quality of the samples. The concentration of Br ion increased from the bottom to the top with a decrease in the diffraction angle of the (001) plane. The distance between the (001) plane was calculated using the Scherrer equation [Fig. 2(b)]. The ionic radius of the Br ion (0.196 nm) is smaller than that of the I ion (0.206 nm). Hence, the (001) plane distance of $(BA)_2PbI_4$ (1.377 nm) increased in $(BA)_2PbBr_4$ (1.387 nm).[41] The (00*l*) peaks did not increase linearly with an increase in the amount of Br. However, the substitution of I by a small amount of Br ion increased the (00*l*) peaks abnormally. This unusual trend is different from the previously reported $(BA)_2Pb(Br–I)_4$ single crystals, but similar to that for $(PEA)_2PbX_4$ (X = Br, I) single crystals[42] and $(PEA)_2Pb(Br–I)_4$ thin films.[43] Thus, the sharp increase in the interlayer separation can be ascribed to the lattice distortion of the octahedral $[PbX_6]^{4-}$.

The crystal structure, morphology, and phase purity of the synthesized samples were further detected using HR-TEM, FE-SEM, and EDS, respectively. Fig. 2(c) shows the HR-TEM

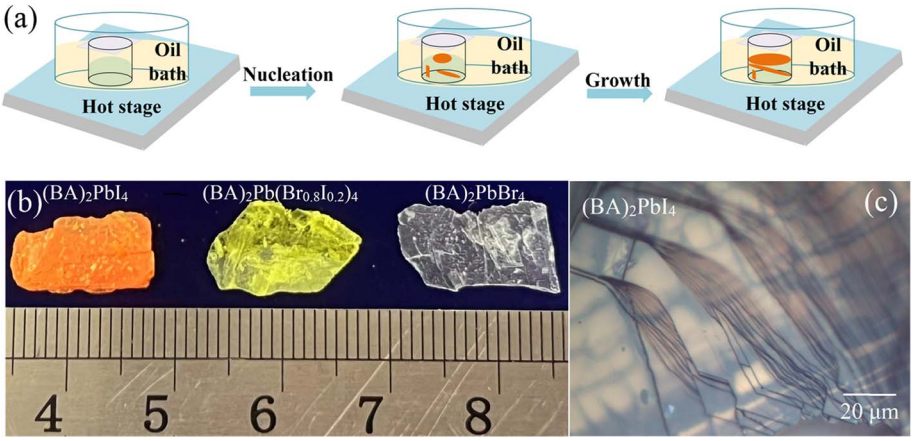

Fig. 1 (a) Schematic of the procedure to grow the mixed halide 2D perovskite $(BA)_2Pb(Br_xI_{1-x})_4$ single crystals. (b) $(BA)_2PbI_4$, $(BA)_2Pb(Br_{0.8}I_{0.2})_4$, and $(BA)_2PbBr_4$ single crystals (from left to right). (c) $(BA)_2PbI_4$ single crystal.

image of $(BA)_2Pb(Br_{0.35}I_{0.65})_4$. The lattice spacing of 0.30 nm corresponds to the perovskite (010) plane, where the regular crystal structure proves the high quality of the $(BA)_2Pb(Br_{0.35}I_{0.65})_4$ single crystal. The surface morphology of $(BA)_2Pb(Br_{0.35}I_{0.65})_4$ analyzed by FE-SEM is shown in Fig. 2(d). The sample surface is uniform and smooth on a 30 × 30 μm

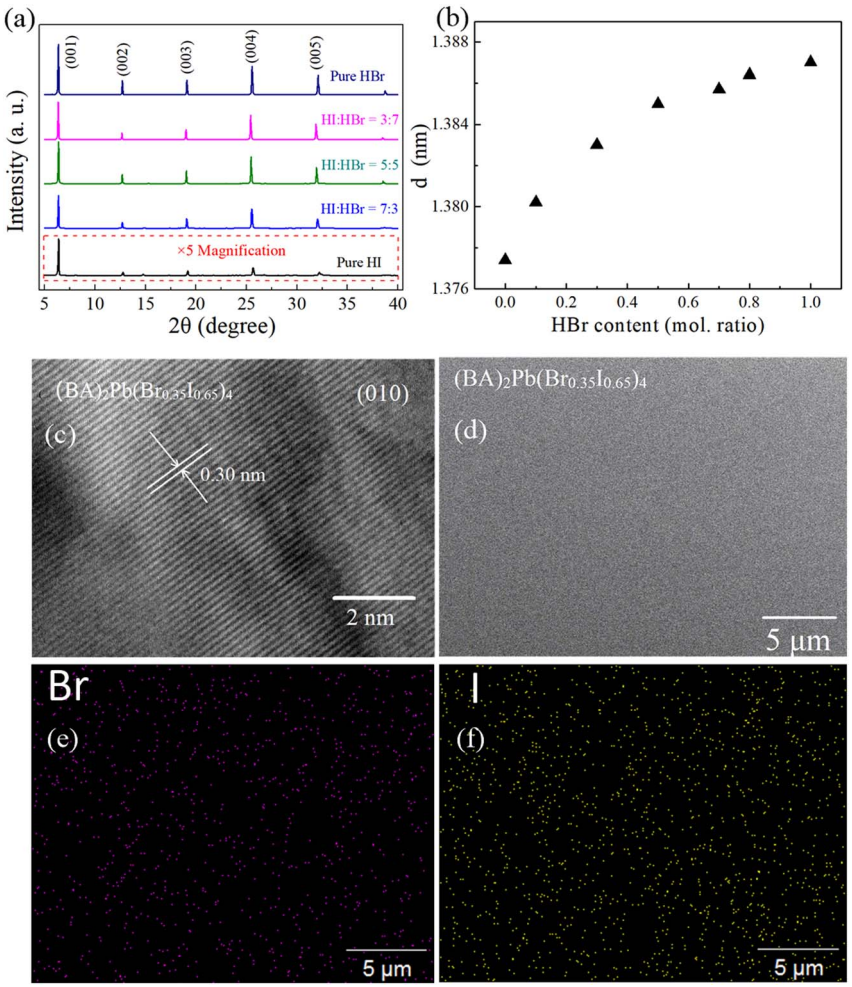

Fig. 2 (a) XRD patterns of $(BA)_2Pb(Br_xI_{1-x})_4$ single crystals. (b) Distance of the (001) plane calculated according to the Scherrer equation. (c) HR-TEM image of the $(BA)_2PbI_4$ single crystal. (d) FE-SEM image of $(BA)_2Pb(Br_{0.35}I_{0.65})_4$. EDS element scanning measurement of $(BA)_2Pb(Br_{0.35}I_{0.65})_4$ of (e) Br and (f) I.

scale. EDS detected the element distribution of the Br and I ion in the mixed halide alloy of $(BA)_2Pb(Br_{0.35}I_{0.65})_4$, and the results are shown in Fig. 2(e) and (f), respectively. The uniform distribution of Br and I in the sample indicates that $(BA)_2Pb(Br_{0.35}I_{0.65})_4$ is a single-phase alloy.

3.2 Chemical composition

In previous reports,[25,34,35,44,45] the halide content in MHPs was assumed to be the same as that in the precursor solutions and the small composition deviation was ignored, which might have introduced errors in the study of MHP alloys. Consequently, the composition of the products would be inaccurate due to the ignored deviation and the decision on property would be incorrect given that the property of MHPs highly depends on their composition. We measured the chemical composition of the prepared $(BA)_2Pb(Br_xI_{1-x})_4$ in this work using XPS, especially the atomic ratio of I and Br in the synthesized crystals. The binding energy of the 3d electrons of I and Br of all the samples is shown in Fig. 3(a). With an increase in the mole ratio of HBr and HI in the precursor solutions, the intensity of the 3d peak of I decreased, while the intensity of the 3d peak of Br increased. This proves that the Br ion entered the $[PbX_6]^{4-}$ octahedral structure and replaced the I ion. The 3d lines of Br and I in $(BA)_2Pb(Br_xI_{1-x})_4$ were studied to explore the valence state of the halide ions, and the results are shown in Fig. 3(b) and (c), respectively. The XPS spectra of Br 3d and I 3d were fitted using Gaussian curves. The results indicate that Br and I have a valence state of −1. Therefore, the atomic ratio of Br and I in the perovskite crystals can be calculated by comparing the peak area of the 3d orbitals of Br and I. Fig. 3(d) presents a comparison of the halide contents of the crystals and their precursor solutions. The Br content in the crystals is lower than that in their solutions, whereas the I content is higher. The XPS results demonstrated that it was difficult for the Br ion to be incorporated in the $[PbI_6]^{4-}$ octahedron although it has stronger affinity to combine with Pb^{2+}. It has been proven that the complexation of Pb^{2+}/Br^- occurs before that of Pb^{2+}/I^- when PbI_2 or $PbBr_2$ is dissolved in organic solvents with equimolar concentrations.[46–48] The deviation in the measured and theoretical composition of $(BA)_2Pb(Br_xI_{1-x})_4$ was mainly ascribed to the different ionic radii of the halogens. The ionic radius of Br and I is 0.196 and 0.206 nm, respectively. It has been reported for several other MHPs[49,50] that it is difficult for a smaller halogen ion to be incorporated in the $[PbX_6]^{4-}$ octahedron with a bigger halogen occupying the X site. Notably, we observed a deviation in the halide composition in the 2D MHP SCs from that in their solutions, and this deviation cannot be neglected; otherwise, the relation between composition and property, such bandgap width, of the MHPs would become absurd and confusing.

To verify the above-mentioned result, $(BA)_2Pb(Cl\text{–}Br)_4$ was synthesized in mixed HX (X: Cl, Br) solutions and its composition was measured using XPS. Fig. 4(a) shows the XPS result of $(BA)_2Pb(Cl\text{–}Br)_4$ synthesized in mixed HX (X: Cl, Br) solutions. Fig. 4(b) shows the comparison of the measured and theoretical Cl and Br in $(BA)_2Pb(Cl\text{–}Br)_4$, indicating the deviation in the composition. A marked deviation was observed in $(BA)_2Pb(Cl\text{–}Br)_4$. The atomic ratio of Cl : Br in $(BA)_2Pb(Cl\text{–}Br)_4$ is much less than in the precursor solution. Specifically, 15% of Br was substituted by Cl in the synthesized crystal when HCl : HBr was 9 : 1 in the solution. The ionic radius of Cl (0.181 nm) is much

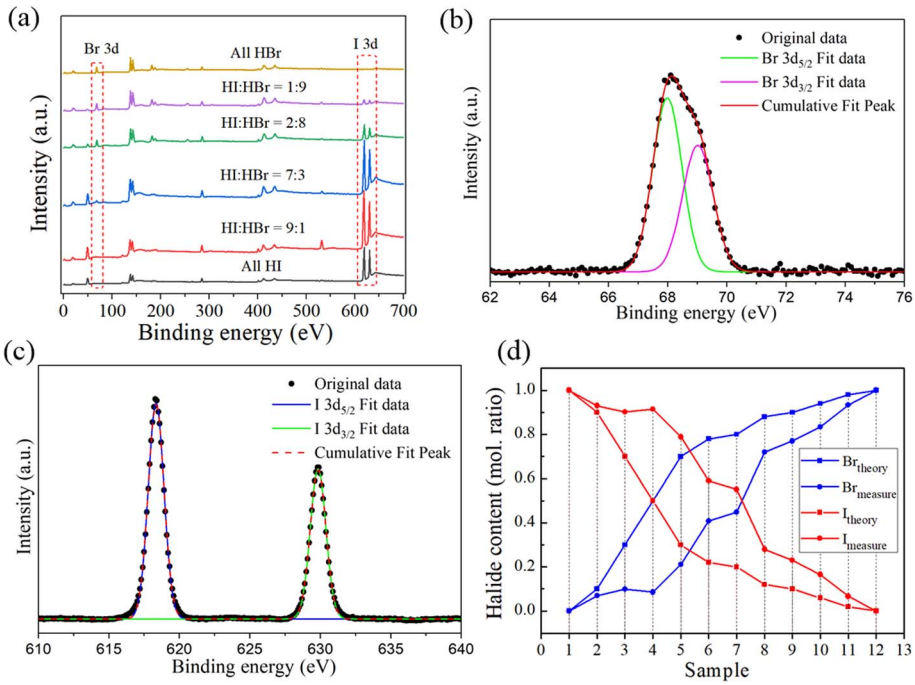

Fig. 3 (a) XPS survey of $(BA)_2Pb(Br_xI_{1-x})_4$ crystals fabricated in mixed HX solutions. (b) Br 3d and (c) I 3d spectra fitted using Gaussian curves. (d) Comparison of the measured and theoretical contents of I and Br in the $(BA)_2Pb(Br_xI_{1-x})_4$ single crystals.

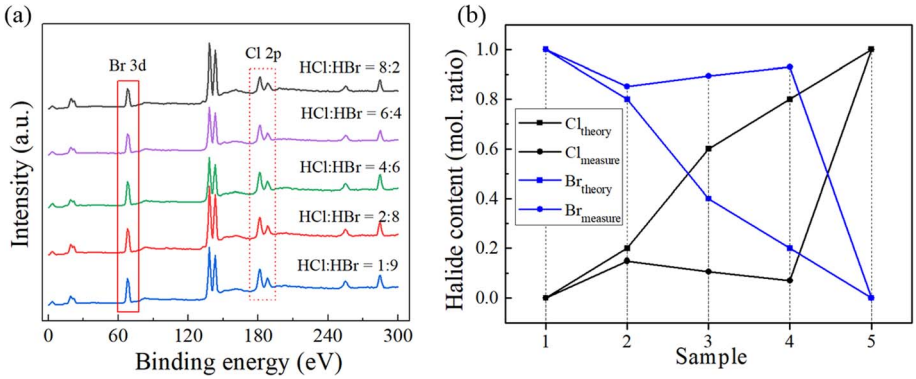

Fig. 4 (a) XPS survey of $(BA)_2Pb(Cl–Br)_4$ fabricated in mixed HX solutions. (b) Comparison of the measured and theoretical contents of Cl and Br in the $(BA)_2Pb(Cl–Br)_4$ single crystals.

smaller than that of Br. The difference in the ionic radius of Cl and Br is 7.6%, where a larger difference in radius would have led to more a severe deviation in composition in the Cl–Br system. Thus, less Cl can be incorporated in the Br-based perovskite lattice $(BA)_2Pb(Cl–Br)_4$. Thus, although single-phase 2D OHP alloys were successfully fabricated using an aqueous solution method, the halide content in the products distinctly deviated from that in the precursor solutions.

3.3 Bandgap

The absorption spectra of $(BA)_2Pb(Br_xI_{1-x})_4$ were investigated to understand the regulation of its bandgap by mixed halides, as shown in Fig. 5(a). The absorption spectra of the samples gradually shifted toward a shorter wavelength with an increase in the Br content, showing a blue shift from 550 to 425 nm. The substitution of I by Br gradually increased the width of the bandgap. The tangent method and the Kubelka–Munk formula were used to calculate the actual change in the bandgap width. The Kubelka–Munk formula is expressed as eqn (1), as follows:

$$F(A) = \left(1 - \frac{1}{10^A}\right)^2 \Big/ \frac{2}{10^A} \quad (1)$$

where A is the absorbance. The Tauc plots corresponding to the absorption spectra were calculated. The graph was plotted considering $h\nu = 1240/\lambda$ as the abscissa and $(Ah\nu)^{1/2}$ as the ordinate [Fig. 5(b)], and a tangent was drawn to the resulting graph to obtain the bandgap width. The calculated bandgap widths of $(BA)_2Pb(Br_xI_{1-x})_4$ are shown in Fig. 5(c), indicating that its bandgap can be tuned by varying the Br/I ratio. However, the bandgap varied nonlinearly with an increase in the content of Br. The variation in E_g can be described as a quadratic function of composition, as follows:

$$E_g[(BA)_2Pb(Br_xI_{1-x})_4] = E_g[(BA)_2PbI_4] + \{E_g[(BA)_2PbBr_4] - E_g[(BA)_2PbI_4] - b\}x + bx^2$$

where b is the bowing parameter. The fitting of the experimental result is

$$E_g = 2.20 + 0.69x + 0.65x^2$$

The bowing parameter of 0.65 eV is small enough to demonstrate that high miscibility was obtained in the single crystal of $(BA)_2Pb(Br_xI_{1-x})_4$.[51,52]

The dual bandgap observed in 2D or quasi 2D perovskites[53–55] was measured for $(BA)_2Pb(Br_xI_{1-x})_4$. However, the origin of the dual bandgap is still debatable. Some authors ascribed it to different structures in 2D perovskites,[53] whereas others to the electron–phonon coupling caused by the local strain in perovskite crystals.[54] The photoluminescence (PL) of

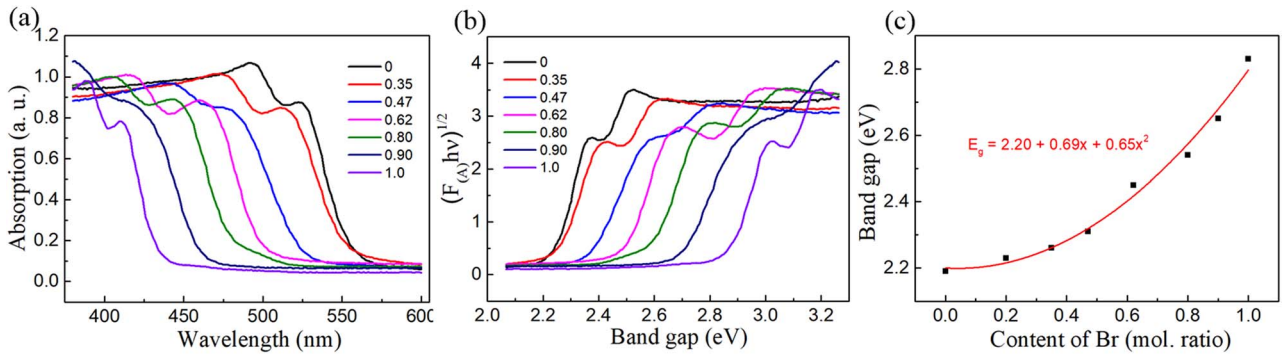

Fig. 5 (a) Absorption spectrum of $(BA)_2Pb(Br_xI_{1-x})_4$ single crystals and (b) corresponding Tauc plot. (c) Relation curve between the band gap and Br composition of $(BA)_2Pb(Br_xI_{1-x})_4$.

$(BA)_2Pb(Br_xI_{1-x})_4$ was measured to clarify its light emission characteristics and the origin of its dual bandgap. The results are shown in the following section.

3.4 Light emission

The PL spectra of $(BA)_2Pb(Br_xI_{1-x})_4$ measured at room temperature of 25 °C are shown in Fig. 6(a). Br doping strongly regulated the emission characteristics of the 2D perovskite crystals, where the light emitted from $(BA)_2Pb(Br_xI_{1-x})_4$ shifted to a shorter wavelength with an increase in the Br content. Interestingly, the emission at a low energy shifted to a shorter wavelength more quickly, and finally resulted in a high-energy emission. The emission at 550 nm disappeared when 0.25 of I was substituted by Br. This indicates that pure light with a unitary wavelength was obtained in the mixed-halide samples compared to the $(BA)_2PbI_4$ and $(BA)_2PbBr_4$ monohalides. The symmetrical shape of the single peak demonstrates that it is not formed by the merger of two peaks. The small PL peak broadening may have been caused by the disorder-induced effects in the mixed-halide perovskite alloy. An important report about layered perovskite alloys confirmed that the 2D excitons present Wannier character rather than Frenkel character due to the disorder-induced effects.[28] Therefore, mixed halides can tune the PL emission from dual peaks to a single broad peak.

The PL of different portions of $(BA)_2Pb(Br_xI_{1-x})_4$ was measured to explore the origin of the dual emission and the influence of lattice distortion on the emission property of the 2D OHPs. $(BA)_2PbI_4$ and $(BA)_2PbI_4$ were split into two, *i.e.*, the surface and bulk, and the PL from these two different parts are shown in Fig. 6(b). According to the results, a high energy emission was obtained from the surface, while a low energy emission was obtained from the bulk. We supported that the electronic interaction between the inorganic layers in a layered perovskite single crystal is the origin of the dual emission.[55] An increase in the distance between the inorganic layers can decrease these electronic interactions. Our experimental results and some important reports offer solid proof for this claim. Firstly, the XRD pattern of $(BA)_2Pb(Br_xI_{1-x})_4$ indicates that a small amount of doped Br sharply increased the *d*-spacing of the (001) plane. This may reduce the stacking effect and electron–photon coupling in the inner region of the crystal and diminish the lower-energy emission. Secondly, the $(PEA)_2PbBr_4$ and $(PEA)_2PbI_4$ crystals were prepared and measured as the reference samples. According to the XRD result in Fig. 6(c), a larger interlayer distance was obtained in the PEA perovskites based on the smaller diffraction angle of the (001) plane. The PL measurement results [Fig. 6(d)] revealed that a single PL peak was detected for the $(PEA)_2PbBr_4$ and $(PEA)_2PbI_4$ samples. The pure light emission of $(BA)_2Pb(Br_xI_{1-x})_4$ was due to the structural homogeneity of the alloyed crystals. Thus, Br doping can improve the light emission purity of 2D I-based perovskite single crystals.

The emission intensity under the same excitation decreased suddenly when 0.8 of I was substituted by Br. We monitored the PL emission of the $x = 0.8$ sample in dozens of positions carefully and a faint blue emission was captured at a few of positions. However, in most of the positions, no emission was

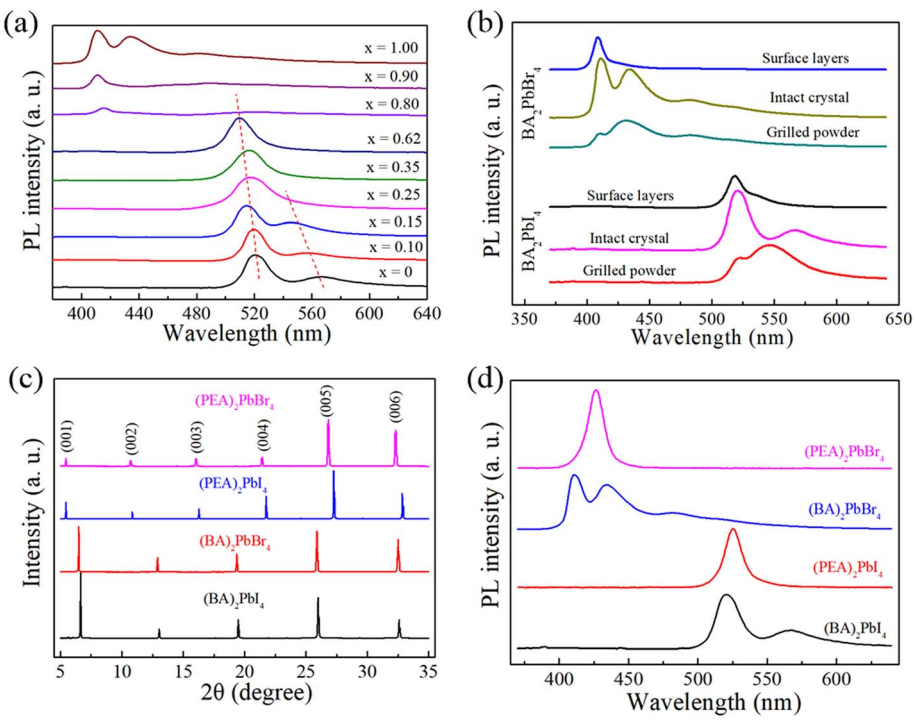

Fig. 6 (a) PL of $(BA)_2Pb(Br_xI_{1-x})_4$ at room temperature of 25 °C with different Br^- compositions. (b) PL of few layers on the surface of $(BA)_2Pb(Br_xI_{1-x})_4$, milled powder of $(BA)_2Pb(Br_xI_{1-x})_4$, and intact crystal. (c) XRD patterns and (d) PL spectra of the $(PEA)_2PbBr_4$, $(PEA)_2PbI_4$, $(BA)_2PbBr_4$ and $(BA)_2PbI_4$ single crystals.

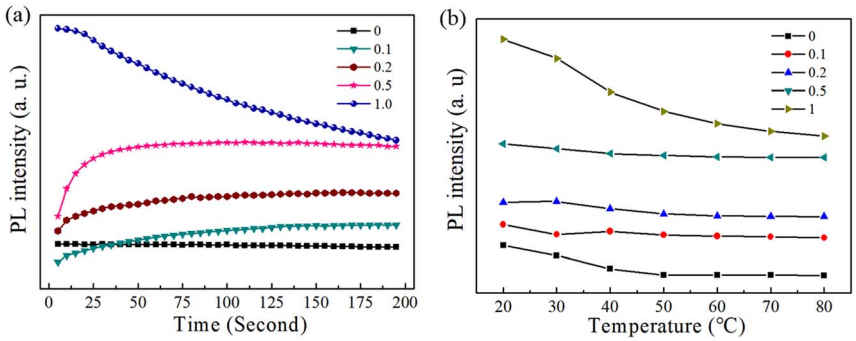

Fig. 7 (a) PL intensity of the $(BA)_2Pb(Br_xI_{1-x})_4$ crystals with time under UV illumination. (b) PL intensity of $(BA)_2Pb(Br_xI_{1-x})_4$ crystals with temperature.

detected. According to the wavelength of the emission, we attributed the faint blue emission to the trace $(BA)_2PbBr_4$ crystals separated from of the MHP alloy. The rich-Br MHPs did not emit light when they were excited by the 310 nm UV light. A similar phenomenon was observed in the $x = 0.9$ sample. The emission degeneration of the rich-Br samples can be ascribed to the inhibition of exciton transport of halide mixing. Michael Seitz *et al.*[56] verified that the random distribution of alloying sites in phase-pure mixed-halide 2D and 3D perovskites can induce an energetically disordered potential in the alloys. The disordered potential inhibited the exciton transport drastically, especially in the Br-rich samples. Thus, combined with the abundant defects induced by the deep deformation of $[PbX_6]^{4-}$, the emission intensity of the Br-rich samples was reduced sharply.

3.5 Stability

The photo and thermal stability of the synthesized $(BA)_2Pb(Br_xI_{1-x})_4$ were measured under UV illumination at high temperatures. Their stability was determined based on the reduction in the absolute PL intensity of the samples. A UV lamp with a wavelength of 275 nm and power of 5 W was used to illuminate the samples to measure their photostability. The PL intensity was recorded using a fluorescence spectrometer and the results are shown in Fig. 7(a). The PL intensity of $(BA)_2PbBr_4$ and $(BA)_2PbI_4$ decreased monotonously with time when exposed to light. However, the mixed-halide $(BA)_2Pb(Br_xI_{1-x})_4$ showed an abnormal increase in PL intensity in the first few seconds, followed by a stable intensity after 200 s. Thus, the $(BA)_2Pb(Br_xI_{1-x})_4$ samples exhibited high photostability after ion migration was completed. The thermal stability of the samples was detected by heating then from 20 °C to 80 °C using a hot stage. With an increase in temperature, a smaller decrease in PL intensity was observed in the $(BA)_2Pb(Br_xI_{1-x})_4$ mixed-halide, as shown in Fig. 7(b). Thus, according to the above-mentioned results, the mixed- $(BA)_2Pb(Br_xI_{1-x})_4$ halide shows higher photo and thermal stability compared to the single-halide $(BA)_2PbBr_4$ crystals.

There are two possible reasons to explain the long-duration photo and thermal stability of the $(BA)_2Pb(Br_xI_{1-x})_4$ mixed-halide. Firstly, the rearrangement of the halide ion caused by the photo-induced ion migration may have donated a low energy state for $(BA)_2Pb(Br_xI_{1-x})_4$. The increase in the PL intensity in the first few seconds under UV light illumination indicated I ion migration. When the photo-induced ion migration was complete, a relatively stable structure was formed in the MHP samples, which contributed the subsequent long-time photo stability of $(BA)_2Pb(Br_xI_{1-x})_4$ effectively. Secondly, halide doping may have increased the stability of the mixed-halide perovskites by enhancing the interaction between the BA moiety and the inorganic cage. It has been reported that the stability of 3D and 2D perovskites is influenced by the interaction between the organic cation and the inorganic framework, where a stronger interaction leads to higher stability.[57,58] Thus, the substitution of I by Br in the mixed-halide samples should have increased the interaction due to the stronger affinity of the Br ion.

4. Conclusion

In this study, centimeter-size, high-quality 2D organic–inorganic perovskite plates with tunable bandgaps and light emission were successfully prepared in a mixed HX (X = Br and I) aqueous solution. The synthesis of the highly efficient luminous crystals was performed using an economically and environmentally friendly method. The structure, composition, and property results indicated the difficulty in controlling the atomic ratio of the halogens in the perovskite products using the solution method because the affinity and the ionic radius of the halogens are different. The substitution of I by Br could tune the lattice and electronic structures of $(BA)_2Pb(Br_xI_{1-x})_4$. An increase in the substituted Br enlarged the (001) plane distance of the 2D perovskite from 1.377 to 1.387 nm. However, the increase in the plane distance was not linear because of the lattice distortion of $[PbX_6]^{4-}$. The distortion regulated the emitted light of the mixed halide 2D perovskite. Pure light was obtained from the $(BA)_2Pb(Br_xI_{1-x})_4$ mixed-halide. Thus, halogen doping improved the purity of the emitted light of the 2D perovskite single crystals. The mixed halide enhanced the thermal and photostability of the 2D perovskite even with ion migration. This study offers an effective pathway to improve the light emission property and stability of 2D OHP-based light-emitting and other optoelectric devices.

Author contributions

Haiyan Wang: investigation, methodology, funding acquisition, writing the first draft, project administration; Qiaohe Wang: methodology, data curation, software; Mengxin Ning: investigation, formal analysis; Sen Li, formal analysis; Renzhong Xue, formal analysis; Peng Chen, formal analysis; Zijiong Li: writing – review & edit.

Conflicts of interest

No conflict of interest exists.

Acknowledgements

This work is supported by Key Research & Development and Promotion Projects in Henan Province (grant numbers 212102210134, 212102210120, 222102210038), as well as Maker Space project in Zhengzhou University of Light Industry (grant number 2021ZCKJ220).

References

1 B. Saparov and D. B. Mitzi, *Chem. Rev.*, 2016, **116**, 4558–4596.
2 K. Wang, J. Y. Park and A. L. Dou, *EcoMat*, 2021, **3**, e12104.
3 K. Tanaka, T. Takahashi, T. Kondo, K. Umeda, K. Ema, *et al.*, *Jpn. J. Appl. Phys.*, 2005, **44**, 5923.
4 M. Tikhodeev and G. Ishihara, *Phys. Rev. B: Condens. Matter Mater. Phys.*, 1995, **51**, 14370.
5 J. Li, L. Luo, H. Huang, C. Ma, Z. Ye, J. Zeng and H. He, *J. Phys. Chem. Lett.*, 2017, **8**, 1161.
6 X. Hong, T. Ishihara and A. J. Nurmikko, *Phys. Rev. B: Condens. Matter Mater. Phys.*, 1992, **45**, 6961.
7 K. Kondo, I. Sasaki and U. Miura, *Phys. Rev. B: Condens. Matter Mater. Phys.*, 1993, **47**, 2010.
8 C. Qin, T. Matsushima, A. S. D. Sandanayaka, Y. Tsuchiya and C. Adachi, *J. Phys. Chem. Lett.*, 2017, **8**, 5415.
9 D. Liang, Y. Peng, Y. Fu, M. J. Shearer, J. Zhang, J. Zhai, Y. Zhang, R. J. Hamers, T. L. Andrew and S. Jin, *ACS Nano*, 2016, **10**, 6897.
10 J. C. Blancon, A. V. Stier, H. Tsai, W. Nie, C. C. Stoumpos, *et al.*, Scaling law for excitons in 2D perovskite quantum wells, *Nat. Commun.*, 2018, **9**, 2254.
11 X. Xiao, J. Dai, Y. Fang, J. Zhao, X. Zheng, S. Tang, P. N. Rudd, X. C. Zeng and J. Huang, *ACS Energy Lett.*, 2018, **3**, 684.
12 I. C. Smith, E. T. Hoke, D. Solis-Ibarra, M. D. McGehee and H. I. Karunadasa, *Angew. Chem., Int. Ed.*, 2014, **53**, 11232.
13 C. M. M. Soe, W. Nie, C. C. Stoumpos, H. Tsai, J.-C. Blancon, F. Liu, J. Even, T. J. Marks, A. D. Mohite and M. G. Kanatzidis, *Adv. Energy Mater.*, 2018, **8**, 1700979.
14 C. Ge, W. Zhai, C. Tian, S. Zhao, T. Guo, S. Sun, W. Chen and G. Ran, *RSC Adv.*, 2019, **9**, 16779.
15 C. Han, Q. Wei, X. Jiang, B. Yao, H. Li, H. Chen, B. Li, P. Fu, W. Zhou and Z. Ning, *ACS Mater. Lett.*, 2022, **4**, 987–994.
16 S. Wang, Y. Chen, J. Yao, G. Zhao, L. Li and G. Zou, *J. Mater. Chem. C*, 2021, **9**, 6498.
17 J. Yukta, M. A. Ghosh, S. Afroz, P. J. Alghamdi, S. Sellin and S. Satapathi, *ACS Photonics*, 2022, **9**, 3529–3539.
18 S. Wang, Y. Yao, Z. Wu, Y. Peng, L. Li and J. Luo, *J. Mater. Chem. C*, 2018, **6**, 12267.
19 L. Mao, Y. Wu, C. C. Stoumpos, B. Traore, C. Katan, J. Even, M. R. Wasielewski and M. G. Kanatzidis, *J. Am. Chem. Soc.*, 2017, **139**, 11956–11963.
20 R. M. Kennard, C. J. Dahlman, J. Chung, B. L. Cotts, A. A. Mikhailovsky, *et al.*, *Chem. Mater.*, 2021, **33**, 7290–7300.
21 H. Tsai, W. Nie, J.-C. Blancon, C. C. stoumpos, R. Asadpour, *et al.*, *Nature*, 2016, **536**, 312–316.
22 B.-E. Cohen, T. Binyamin, T. Ben-Tzvi, O. Goldberg, A. Schlesinger, I. Balberg, O. Millo, E. Gross, D. Azulay and L. Etgar, *ACS Energy Lett.*, 2022, **7**, 217–225.
23 X. Li, X. Lian, J. Pang, B. Luo, Y. Xiao, M.-D. Li, X.-C. Huang and J. Z. Zhang, *J. Phys. Chem. Lett.*, 2020, **11**, 8157–8163.
24 M. Mączka, J. K. Zaręba, A. Gągor, D. Stefańska, M. Ptak, K. Roleder, *et al.*, *Chem. Mater.*, 2021, **33**, 2331–2342.
25 B. Slimi, M. Mollar, I. Ben Assaker, A. Kria, R. Chtourou and B. Mari, *Monatsh. Chem.*, 2017, **148**, 835–844.
26 B. A. Rosales, M. P. Hanrahan, B. W. Boote, A. J. Rossini, E. A. Smith and J. Vela, *ACS Energy Lett.*, 2017, **2**, 906–914.
27 S. J. Yoon, K. G. Stamplecoskie and P. V. Kamat, *J. Phys. Chem. Lett.*, 2016, **7**, 1368–1373.
28 G. Lanty, J. Kemli, Y. Wei, J. Leymarie, J. Even, J. S. Lauret and E. Deleporte, *J. Phys. Chem. Lett.*, 2014, **5**, 3958–3963.
29 S. Meloni, G. Palermo, N. Ashari-Astani, M. Grätzel and U. Rothlisberger, *J. Mater. Chem. A*, 2016, **4**, 15997–16002.
30 B. A. Rosales, L. Men, S. D. Cady, M. P. Hanrahan, A. J. Rossini and J. Vela, *Chem. Mater.*, 2016, **28**, 6848–6859.
31 F. Brivio, C. Caetano and A. Walsh, *J. Phys. Chem. Lett.*, 2016, **7**, 1083–1087.
32 R. Gautier, M. Paris and F. Massuyeau, *J. Am. Chem. Soc.*, 2019, **141**, 12619–12623.
33 L. Mao, Y. Wu, C. C. Stoumpos, B. Traore, C. Katan, J. Even, M. R. Wasielewski and M. G. Kanatzidis, *J. Am. Chem. Soc.*, 2017, **139**, 11956–11963.
34 A. Yangui, S. Pillet, A. Lusson, E.-E. Bendeif, S. Triki, Y. Abid and K. Boukheddaden, *J. Alloys Compd.*, 2017, **699**, 1122–1133.
35 S. Wang, Y. Yao, Z. Wu, Y. Peng, L. Li and J. Luo, *J. Mater. Chem. C*, 2018, **6**, 12267–12272.
36 Y. Han, J. Yin, G. Cao, Z. Yin, Y. Dong, R. Chen, Y. Zhang, N. Li, S. Jin, O. F. Mohammed, B.-B. Cui and Q. Chen, *ACS Energy Lett.*, 2022, **7**, 453–460.
37 P. S. Mathew, J. T. DuBose, J. Cho and P. V. Kamat, *ACS Energy Lett.*, 2021, **6**, 2499–2501.
38 M. Rahil, P. Rajput, D. Ghosh and S. Ahmad, *ACS Appl. Electron. Mater.*, 2020, **2**, 3199–3210.
39 Z. Huang, A. H. Proppe, H. Tan, M. I. Saidaminov, F. Tan, A. Mei, C.-S. Tan, M. Wei, Y. Hou, H. Han, S. O. Kelley and E. H. Sargen, *ACS Energy Lett.*, 2019, **4**, 1521–1527.
40 Y. Nah, O. Allam, H. S. Kim, J. Choi, I. S. Kim, J. Byun, S. O. Kim, S. S. Jang and D. H. Kim, *ACS Nano*, 2021, **15**, 1486–1496.
41 Q. Dong, Y. B. Yuan, Y. C. Shao, Y. J. Fang, Q. Wang and J. S. Huang, *Energy Environ. Sci.*, 2015, **8**, 2464.

42 D. Ma, Y. Fu, L. Dang, J. Zhai, I. A. Guzei and S. Jin, *Nano Res.*, 2017, **10**, 2117–2129.
43 N. Kitazawa, *Mater. Sci. Eng., B*, 1997, **49**, 233–238.
44 H. He, G. Tong, Y. Shi, R. Wang, Y. Liu, J. Chen, N. Thirugnanam, J. Chen and Y. He, *J. Mater. Res. Technol.*, 2021, **15**, 5353–5359.
45 N. E. Wright, X. Qin, J. Xu, L. L. Kelly, S. P. Harvey, M. F. Toney, V. Blum and A. D. Stiff-Roberts, *Chem. Mater.*, 2022, **34**, 3109–3122.
46 L. Atourki, E. Vega, B. Marí, M. Mollar, H. Ait Ahsaine, K. Bouabid and A. Ihlal, *Appl. Surf. Sci.*, 2016, **371**, 112–117.
47 Y. Dou, F. Cao, T. Dudka, Y. Li, S. Wang, C. Zhang, Y. Gao, X. Yang and A. L. Rogach, *ACS Mater. Lett.*, 2020, **2**, 814–820.
48 C. Kaewmeechai, Y. Laosiritaworn and A. P. Jaroenjittichai, *Results Phys.*, 2022, **42**, 106015.
49 E. L. Unger, A. R. Bowring, C. J. Tassone, V. L. Pool, A. Gold Parker, *et al.*, *Chem. Mater.*, 2014, **26**, 7158.
50 Q. Dong, Y. B. Yuan, Y. C. Shao, Y. J. Fang, Q. Wang and J. S. Huang, *Energy Environ. Sci.*, 2015, **8**, 2464.
51 R. Hill, Energy-gap variations in semiconductor alloys, *J. Phys. C: Solid State Phys.*, 2001, **7**, 521.
52 R. Venugopal, P. I. Lin and Y. T. Chen, *J. Phys. Chem. B*, 2006, **110**, 11691–11696.
53 T. Sheikh, A. Shinde, S. Mahamuni and A. Nag, *ACS Energy Lett.*, 2018, **3**, 2940–2946.
54 Q. Du, C. Zhu, Z. Yin, G. Na, C. Cheng, Y. Han, N. Liu, X. Niu, H. Zhou, H. Chen, L. Zhang, S. Jin and Q. Chen, *ACS Nano*, 2020, **14**, 5806–5817.
55 T. Sheikh, V. Nawale, N. Pathoor, C. Phadnis, A. Chowdhury and A. Nag, *Angew. Chem., Int. Ed.*, 2020, **132**, 11750–11756.
56 M. Seitz, M. Meléndez, P. York, D. A. Kurtz, A. J. Magdaleno, N. Alcázar-Cano, A. S. Kshirsagar, M. K. Gangishetty, R. Delgado-Buscalioni, D. N. Congreve and F. Prins, *ACS Energy Lett.*, 2022, **7**, 358–365.
57 A. Mohanty, D. Swain, S. Govinda, T. N. Guru Row and D. D. Sarma, *ACS Energy Lett.*, 2019, **4**, 2045–2051.
58 T. Debnath, D. Sarker, H. Huang, Z.-K. Han, A. Dey, L. Polavarapu, S. V. Levchenko and J. Feldmann, *Nat. Commun.*, 2021, **12**, 2629.